Generation of Internal Waves by Eddies Impinging on the Western Boundary of the North Atlantic

L. CLÉMENT* AND E. FRAJKA-WILLIAMS

National Oceanography Centre, University of Southampton, Southampton, United Kingdom

K. L. SHEEN

National Oceanography Centre, University of Southampton, Southampton, United Kingdom, and Met Office Hadley Centre, Exeter, United Kingdom

J. A. BREARLEY

British Antarctic Survey, Cambridge, United Kingdom

A. C. NAVEIRA GARABATO

National Oceanography Centre, University of Southampton, Southampton, United Kingdom

(Manuscript received 26 November 2014, in final form 12 January 2016)

ABSTRACT

Despite the major role played by mesoscale eddies in redistributing the energy of the large-scale circulation, our understanding of their dissipation is still incomplete. This study investigates the generation of internal waves by decaying eddies in the North Atlantic western boundary. The eddy presence and decay are measured from the altimetric surface relative vorticity associated with an array of full-depth current meters extending ~100 km offshore at 26.5°N. In addition, internal waves are analyzed over a topographic rise from 2-yr high-frequency measurements of an acoustic Doppler current profiler (ADCP), which is located 13 km offshore in 600-m deep water. Despite an apparent polarity independence of the eddy decay observed from altimetric data, the flow in the deepest 100 m is enhanced for anticyclones ($25.2 \, \mathrm{cm \, s^{-1}}$) compared with cyclones ($-4.7 \, \mathrm{cm \, s^{-1}}$). Accordingly, the internal wave field is sensitive to this polarity-dependent deep velocity. This is apparent from the eddy-modulated enhanced dissipation rate, which is obtained from a finescale parameterization and exceeds $10^{-9} \, \mathrm{W \, kg^{-1}}$ for near-bottom flows greater than $8 \, \mathrm{cm \, s^{-1}}$. The present study underlines the importance of oceanic western boundaries for removing the energy of low-mode westward-propagating eddies to higher-mode internal waves.

1. Introduction

Mesoscale eddies are ubiquitous across the ocean, with typical length scales of $O(10–100) \, \mathrm{km}$ and time scales of days to months at mid- and high latitudes.

Eddies redistribute the energy input to the ocean by wind stress (~1 TW; Wunsch 1998), which is extracted from the general circulation via baroclinic and barotropic instabilities (Gill et al. 1974; Vallis 2006) and ultimately dissipated through small-scale turbulence. Quantification and mechanistic understanding of the link between mesoscale eddies and small-scale turbulence is key to determining the ocean's energy budget and the role of turbulent flows in shaping the large-scale ocean circulation, yet this link is presently surrounded by many uncertainties and open questions.

The chaotic behavior of eddies, which may interact, merge, disappear, and reappear, hinders observations of

---

* Current affiliation: Lamont-Doherty Earth Observatory, Columbia University, Palisades, New York.

Corresponding author address: Louis Clément, Lamont-Doherty Earth Observatory, Columbia University, 61 Route 9W, P.O. Box 1000, Palisades, NY 10964.
E-mail: lclement@ldeo.columbia.edu

their dissipative processes. According to geostrophic turbulence theory, which assumes no lateral boundaries, frictional bottom drag is the primary dissipation mechanism of mesoscale eddy energy. In this idealized view, energy is input to the first baroclinic mode at the largest scales in the ocean, then transfers to the barotropic mode at a horizontal scale close to the Rossby radius of deformation and is subsequently transported to larger horizontal and vertical scales through an inverse cascade (Salmon 1978). Recent altimetric observations call aspects of this cascade into question (Scott and Wang 2005), while estimates of the rate of dissipation of the oceanic geostrophic flow by bottom drag are subject to large uncertainties (0.2–0.8 TW; Sen et al. 2008). The possible significance of lateral boundaries in eddy dissipation is highlighted by Zhai et al. (2010), who use altimetric measurements to estimate the eddy energy sink (0.1–0.3 TW) at the western boundary of ocean basins. The mechanisms of eddy dissipation at western boundaries are not addressed by that work, and generally, the physical processes underpinning eddy dissipation in the ocean remain poorly understood (Ferrari and Wunsch 2009).

Some mechanisms by which energy can be drained from the mesoscale eddy field are through the intensification and generation of internal waves, which promote dissipation and diapycnal mixing upon breaking. The process of a wave packet captured by an eddy strain field (Bühler and McIntyre 2005; Polzin 2008, 2010) can contribute to their energy exchange without any dependence on the topography. Additionally, internal waves may be generated when a geostrophic current flows over rough topography (Liang and Thurnherr 2012; Brearley et al. 2013) in a process described by the linear theory of lee waves over small-scale abyssal hills (Bell 1975). For steeper and taller topography, nonlinearities arise (Baines 1995; Klymak et al. 2010) that render the energy transfer from geostrophic flow to internal waves less predictable.

The generation of lee waves and their effect on the diapycnal mixing were anticipated in the Southern Ocean by Naveira Garabato et al. (2004). They were further confirmed by analyzing the topography interaction with geostrophic flow (Nikurashin and Ferrari 2010), frontal regions (St. Laurent et al. 2012), and jets of the Antarctic Circumpolar Current (Sheen et al. 2013; Waterman et al. 2013). Because both the strong eddy flow and the enhanced eddy energy loss of disappearing eddies are present at western boundaries, the interplay of eddies with internal waves needs to be studied in those regions. In addition, at western boundaries, other mechanisms may contribute to the internal wave field.

Internal waves may be radiated by hydraulic jumps resulting from the interaction of strong northward flow with Kelvin waves (Hogg et al. 2011). The mixing at western boundaries is also affected by the interaction of deep western boundary currents with the topography (Köhler et al. 2014).

In this study, we investigate eddy decay processes and internal wave generation using a combination of satellite altimetric and in situ current meter observations. These observations are of the western boundary of the North Atlantic, where first baroclinic mode eddies propagate westward from open-ocean waters to the continental slope (Clément et al. 2014). We find evidence of an energization of the internal wave field over the slope as anticyclonic eddies impinge on the western boundary.

2. Data and methods

a. The western boundary

The topography (of depth D) at the western boundary of the RAPID array (Cunningham et al. 2007) at 26.5°N is displayed in Fig. 1. The steep continental slope east of Great Abaco at 26.5°N deepens from 200 to 4500 m over 25 km (76.93°–76.68°W). The focus of our study is the topographic rise of the Bahamas escarpment, which is 21 km long and 1470 m tall (of height H) as defined by the 2000-m isobath (Fig. 1b). Two escarpments, with minimum depths of 1600 m at 26.63° and 26.73°N, deflect the southward deep flow close to topography (Johns et al. 2008). In the top 1000 m, the Antilles Current completes the northward transport of the subtropical gyre (Lee et al. 1996) along with the Gulf Stream, which flows in the Florida Straits. The intense mean Antilles Current ($>40\,\mathrm{cm\,s}^{-1}$ at 400 m) flows around the Bahamas within 110 km of the boundary (Bryden et al. 2005) and is also affected by eddies (Frajka-Williams et al. 2013).

Mooring-based observations at 26.5°N from May 2010 to November 2011 are analyzed here to investigate subsurface variability. The data considered are from five moorings, denoted Wba, Wb1, Wb2, Wb3, and Wb4 and located at 13, 17, 25, 49, and 108 km from the coast in water depths of 595, 1394, 3796, 4840, and 4713 m, respectively (Fig. 1). Current meters on Wb1–4 sampled every 30 min (Johns et al. 2008). One broadband (75 kHz) upward-looking acoustic Doppler current profiler (ADCP) was deployed at Wba (26.53°N, 76.87°W). Velocities are estimated every 30 min in 16-m bins from the instrument depth at 595 to 59 m. Barotropic velocities are calculated as the vertically averaged velocity, and the baroclinic velocity profile is defined as
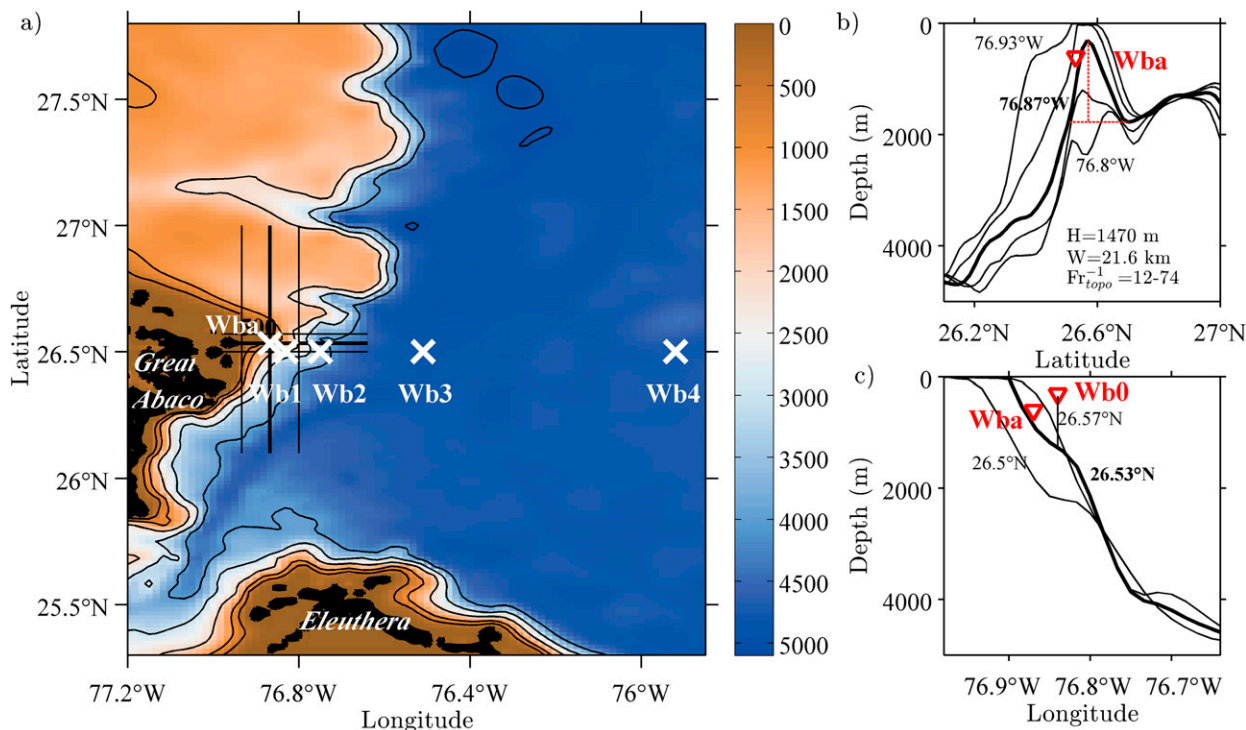
FIG. 1. (a) Bathymetry of the western boundary of the North Atlantic around 26.5°N with Great Abaco and Eleuthera island. The mooring array (Wba, Wb1, Wb2, Wb3, and Wb4) is marked by white crosses. The black bold vertical and thin lines indicate the 1D cross sections around Wba displayed (b) across the longitude 76.87°W (between 76.93° and 76.8°W) and (c) across the latitude 26.53°N (between 26.5° and 26.57°N). The ADCP Wb0 is also located in the longitudinal section (c). The bathymetry is extracted from ETOPO1 provided by NOAA.

the anomaly relative to this mean at each time step. Meridional velocities are bandpassed using a fourth-order Butterworth zero-phase filter used in both forward and reverse directions. Another broadband (150 kHz) upward-looking ADCP Wb0, which only overlaps with Wba for the last 7 months, is analyzed. Wb0 is located 16 km offshore (26.51°N, 76.84°W) at 300 m on a mooring in 1000-m-deep water (Fig. 1c) and measures velocity in 8-m bins from 55 to 300 m.

Hydrographic observations from nine cruises (2006–12) of the Western Boundary Time Series (WBTS) program are used to estimate an average buoyancy frequency profile $N(z)$ with a value of $4 \times 10^{-1} \, s^{-1}$ in the bottommost 100 m at Wba. Data were retrieved from NOAA (ftp://ftp.aoml.noaa.gov/phod/pub/WBTS/Global_Class/). The description of the pre-cruise calibrations, data acquisition, and processing are available on the data portal. Sea surface height anomalies (SSHAs) and surface geostrophic currents are produced by Ssalto/Duacs and distributed by AVISO, with support from CNES (http://www.aviso.altimetry.fr/duacs/). The weekly reference delayed time product mapped to a 1/3° Mercator grid is used. Daily wind speeds at 10 m height are taken from the 1/2° global atmospheric

reanalysis ERA-Interim (http://apps.ecmwf.int/datasets/data/interim-full-daily/; Dee et al. 2011). Zonal and meridional components of wind stress are selected at the closest data point to Wba, at 26.5°N, 76.5°W.

b. Finescale parameterization of turbulent energy dissipation

The measured vertical shear of the internal wave field is used in a finescale parameterization to estimate the rate of dissipation of turbulent kinetic energy, ε (Gregg 1989; Polzin et al. 2014). The parameterization describes the energy transfer from internal waves of large vertical scales [$O(100)$ m] to waves of smaller scales [$O(10)$ m] via wave–wave interactions, as modeled by Henyey et al. (1986). At small scales, the waves break and dissipate energy at a similar rate to that of energy transfer into those scales. The parameterization is based on a comparison of the observed shear spectral variance to that in the Garrett and Munk (GM) model (Gregg and Kunze 1991), which represents the background internal wave field in the open ocean. Variable ε is computed from the finescale parameterization following Gregg et al. (2003), using the shear-to-strain variance ratio (R_ω), $h_1(R_\omega)$, and a latitudinal correction term [$j(f/n)$], such that

$$\varepsilon = \varepsilon_0 \frac{N^2}{N_0^2} \frac{\langle V_z^2 \rangle^2}{\langle V_z^2 \rangle_{\mathrm{GM}}^2} h_1(R_\omega) j(f/N), \tag{1}$$

where $\varepsilon_0 = 6.73 \times 10^{-10}\,\mathrm{W\,kg^{-1}}$ is the reference GM dissipation rate and N_0 is the GM stratification of $5.24 \times 10^{-3}\,\mathrm{s^{-1}}$. The shear-to-strain variance ratio describes the internal waves' aspect ratio and frequency content (Polzin et al. 1995). This is set conservatively, compared to GM ($R_\omega^{\mathrm{GM}} = 3$), to 7 (Kunze et al. 2006). The buoyancy frequency–normalized shear variance $\langle V_z^2 \rangle$ is calculated as the integrated buoyancy frequency–normalized shear spectrum in vertical wavenumber space. The diapycnal eddy diffusivity K_ρ is estimated from the dissipation rate ($K_\rho = \Gamma \varepsilon / N^2$) following Osborn (1980) with a mixing efficiency Γ of 0.2.

3. Results

a. Eddy impingement on the western boundary

The evolution of an anticyclone–cyclone pair as it approaches the western boundary is displayed in Fig. 2. The anticyclone (radius ~125 km) is constrained one month after its arrival at the boundary by Great Abaco to the west and Eleuthera island to the south in late July 2010 (Fig. 2a). One month later, the radius has reduced (~75 km) and the eddy has deformed, perhaps under the influence of incoming propagating features from the east (Fig. 2b). By late September, the anticyclone has almost disappeared and has been replaced by a cyclone of northeastern origin (Fig. 2c). From the altimetric observations, it appears that eddy decay is independent of eddy polarity.

As the cyclone approaches the boundary (from Fig. 2b to 2c), the surface geostrophic velocities accelerate along with intensified SSHAs in the reduced eddy area. The offshore side of the previous anticyclone decays less effectively than its inshore side (Fig. 2b), and it contributes to amplifying the incoming cyclonic inshore edge in the frontal region between those eddies of opposite polarities. The incoming eddy may extract some energy from the decaying eddy through frontal intensification, which is independent to the eddy polarity.

The mooring array complements altimetry by providing subsurface velocity profiles (Figs. 2d–f). Velocities are surface intensified across the section and particularly west of Wb3, where shallower instruments are available. At Wba, the anticyclone has a maximum midwater velocity exceeding $50\,\mathrm{cm\,s^{-1}}$ at the inshore eddy edge, while the cyclone has a maximum southward velocity around $-5\,\mathrm{cm\,s^{-1}}$. The asymmetry between cyclones and anticyclones is consistent with the principle of potential vorticity conservation in shoaling water.

Over the 18-month deployment of Wba, altimetry-derived relative vorticity, velocity, and kinetic energy reveal the differences between cyclones and anticyclones and their evolution through time (Fig. 3). The surface relative vorticity normalized by the planetary vorticity (ζ/f in Fig. 3a) identifies three anticyclones (A1, A2, and A3) and two cyclones (C1 and C2). The relative vorticity is calculated at Wb4 within 1° of latitude and longitude to detect eddies with diameter of up to ~100 km in the vicinity of the array (Fig. 2b). These eddies stayed at the boundary for a relatively long period of ~(2–3) months, as estimated from the sign change of ζ/f and confirmed by the presence of eddies with a radius larger than ~50 km in SSHA maps at the western boundary. The eddies have a mean Rossby number of 0.05–0.1 characteristic of mesoscale features. The vertical structure of velocity shows that anticyclones are strongly barotropic in the meridional direction, with a mean flow of $25.2\,\mathrm{cm\,s^{-1}}$ in the bottommost 100 m. In turn, cyclones are surface intensified, with a near-bottom mean flow of $-4.7\,\mathrm{cm\,s^{-1}}$ (Fig. 3b). The shallow northward Antilles Current observed in the region (Bryden et al. 2005) may contribute to the asymmetric vertical structure of anticyclones and cyclones. Accordingly, anticyclones at Wba are more energetic than cyclones and exhibit peak values of kinetic energy one month after their arrival at the western boundary (Fig. 3d).

b. Eddy-induced modulation of the internal wave field

1) DEPENDENCE OF THE INTERNAL WAVE FIELD ON EDDY POLARITY

In the previous section, we quantified the mesoscale variability from altimetric and low-pass-filtered velocities. We now investigate the internal wave activity using 2D shear spectra and cumulative shear spectra in the presence of these eddies. Shear is normalized by buoyancy frequency before calculating the vertical wavenumber–frequency spectra as $S_{k_z-f}[u_z/N] + S_{k_z-f}[v_z/N]$, where $S_a[b]$ denotes the spectrum of b as a function of a. Spectra are shown in Fig. 4 for both eddy polarities, where the polarity is determined by the sign of the surface relative vorticity. Spectra are calculated in frequency space with 7-day 50% overlapping block averaged for each anticyclone and cyclone (A1, A2, A3, C1, and C2). These in turn are averaged to show typical spectra for anticyclones and cyclones (Figs. 4a,b, respectively). To estimate the relative variance of different wavenumbers for each frequency band, the 2D spectra are further integrated across frequency bands (Fig. 5). The positive (negative) vertical wavenumbers correspond
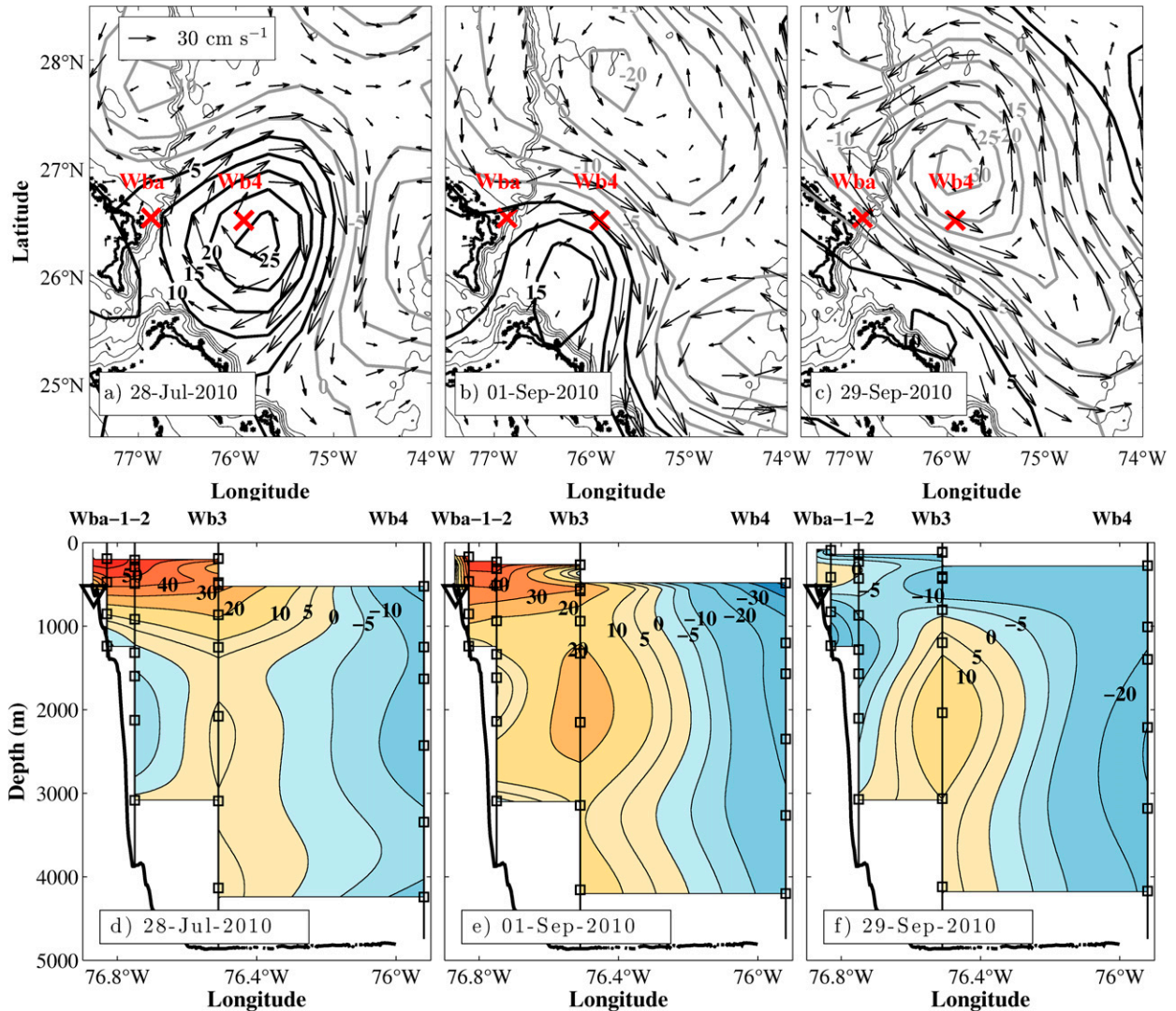
FIG. 2. (top) SSHA (contours; cm) and surface geostrophic currents (arrows; cm s^{-1}) during the decay at the western boundary of one anticyclone from (a) July to (b) September 2010 followed by the arrival of one cyclone (c) a month later. (bottom) Meridional velocity (cm s^{-1}) measured at the same times as (a)–(c) by Wba, Wb1, Wb2, Wb3, and Wb4 during (d),(e) the anticyclone and (f) the cyclone. The black squares mark the positions of the current meters.

in both figures to upward (downward) phase propagation and downward (upward) energy propagation.

Anticyclones show enhanced shear at high frequencies (3–10 h) for negative wavelengths ranging from 67 to 500 m (Fig. 4a) as opposed to positive wavelengths ($\langle V_z^2 \rangle$ is increased by 6%) and to cyclones ($\langle V_z^2 \rangle$ is increased by 40%). This range of the 2D spectra characterizes high-frequency internal waves with downward propagating phase or upward group velocity. In contrast, for cyclones, the asymmetry of the high-frequency shear spectra is less apparent. Similarly, for the near-inertial and M$_2$ tidal bands, there is no asymmetry in the shear spectra related to the vertical wavenumber sign

or to the eddy polarity. At frequencies below the internal wave frequency range, the shear spectrum is larger for anticyclones than cyclones. This low-frequency enhancement across the entire range occurs without a dominant direction of energy propagation.

The integrated 2D shear spectra in frequency (Fig. 5) confirm the enhanced variance of the high-frequency band: for wavelengths larger than 67 m, the shear variance of anticyclones increases by 49% compared with cyclones (considering both signs of vertical wavenumber). This threshold delimits the integration used in the shear variance from 67 to 500 m. Above this wavelength and particularly until 200 m, a strong
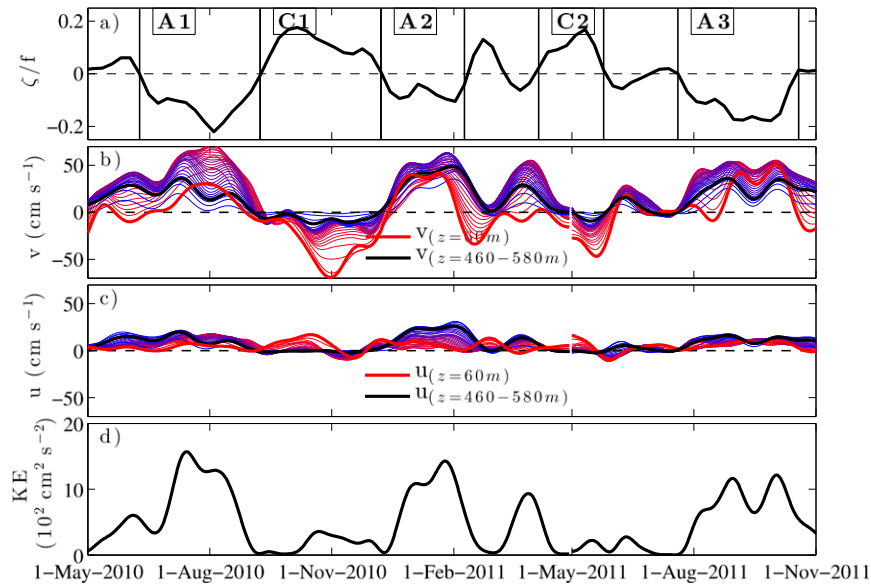
FIG. 3. (a) Surface relative vorticity (ζ/f) within 1° of latitude–longitude of Wb4 normalized by the planetary vorticity. The sign of ζ marks each main anticyclone (A1, A2, and A3) and cyclone (C1 and C2). (b) Meridional and (c) zonal velocity 30-day low-pass filtered at Wba with varying colors representing each depth from 60 (thick red) to 580 m (blue). The thick black line is the bottom-averaged velocity from 460 to 580 m. (d) Depth-averaged (60–580 m) horizontal kinetic energy at Wba.

intensification of high-frequency waves with upward propagating energy is found. Despite no obvious dependence of the shear spectra at the near-inertial and M_2 tidal frequencies in Fig. 4, their shear variance is larger relative to cyclones for vertical wavelengths above 200 and 100 m for the near-inertial and M_2 frequency bands, respectively. The near-inertial signal is characterized by downward propagating energy for anticyclones, consistent with a wind-induced generation. The integrated spectra also highlight energetic
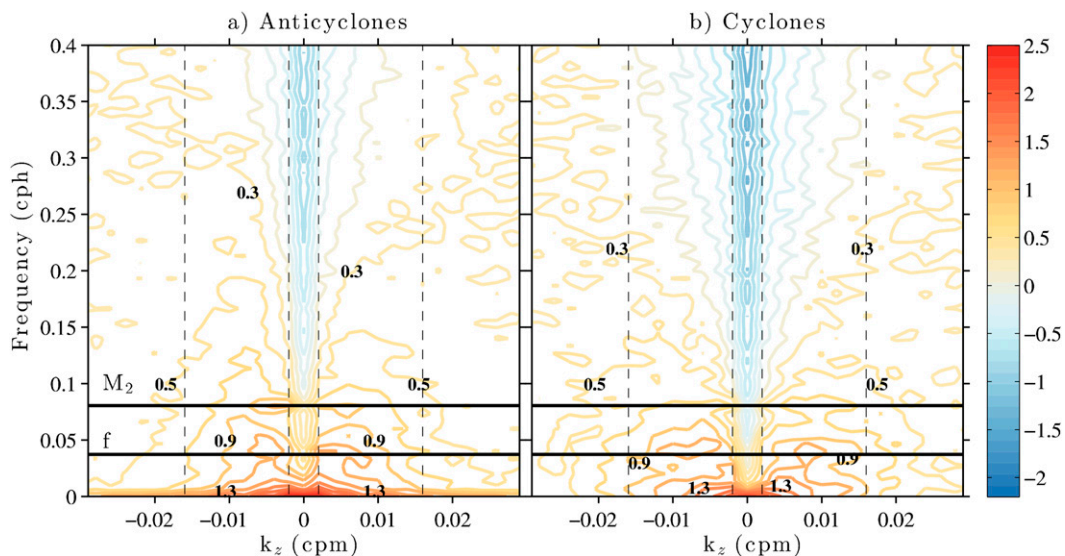

FIG. 4. (a) Vertical wavenumber–frequency spectra of the buoyancy frequency–normalized shear [$\log_{10}$, 1/(cpm × cph)] during (a) anticyclones and (b) cyclones. The M_2 tidal and inertial frequencies are indicated by the thick horizontal black lines. The vertical dashed lines indicate the integration limits of the shear variance.
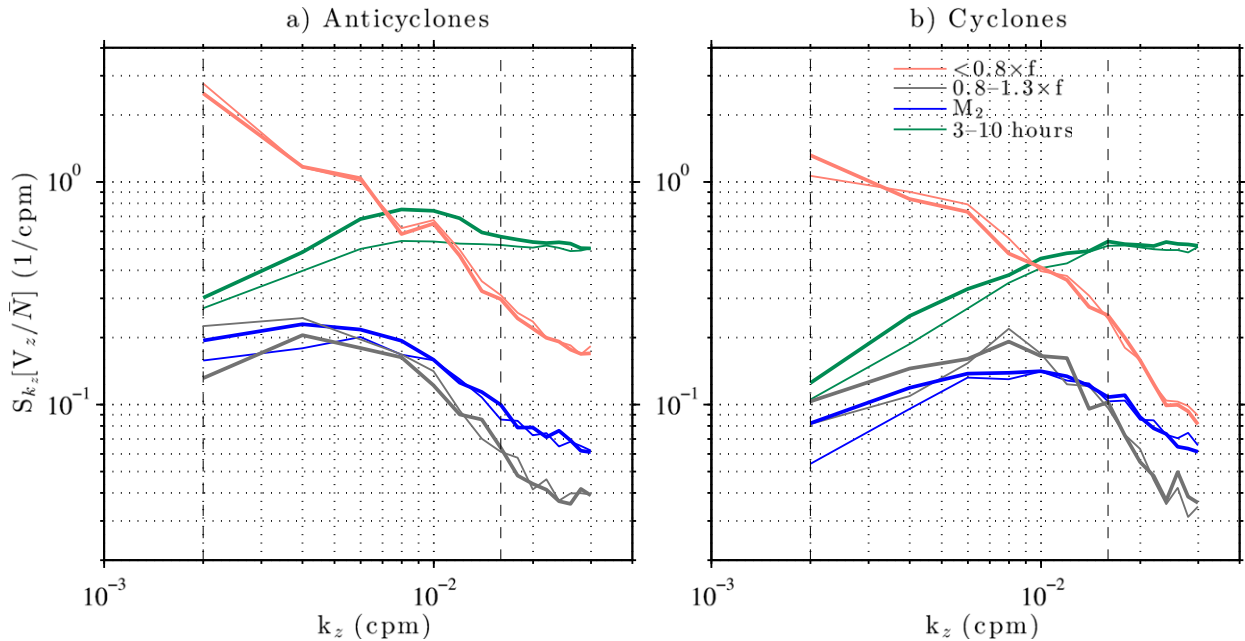
FIG. 5. Integrated 2D spectra of the buoyancy frequency–normalized shear in frequency during (a) anticyclones and (b) cyclones for various frequency bands. The thick (thin) lines represent the negative (positive) vertical wavenumber and upward (downward) energy propagation. The vertical dashed lines indicate the integration limits of the shear variance.

low-frequency shear at low wavenumbers, particularly for anticyclones. This is seen with the red spectra found at low frequencies only.

There is an intensification of high-frequency variance during anticyclones at all depths, evident by comparing the 12-h sampled meridional velocity (Fig. 6b) with the 3–10-h bandpass-filtered meridional velocity (Fig. 6c). The near-inertial [(0.8–1.3) × f; Fig. 6d] band is also slightly energized during anticyclones. However, high-frequency waves contribute more variance than near-inertial waves (Fig. 6e, also apparent in Fig. 5). To estimate the role of the wind stress on the internal wave field, the energy flux into inertial motions is calculated based on the slab model of Pollard and Millard (1970). Following D'Asaro (1985), the energy flux is obtained in Fig. 6a from the mixed layer velocity and the wind stress by considering a constant mixed layer depth of 50 m and an inverse damping parameter of 4 days. With the exception of the intensified near-inertial wave activity in the top 300 m following strong winds (Fig. 6c) from Tropical Storm Otto (October 2010) and Hurricane Irene (September 2011), wind stress is visibly not the main modulator of the internal wave field.

The subinertial shear displays the largest contribution to the shear variance (Fig. 6e) and is also modulated by the presence of anticyclones. The enhanced variance can be attributed not only to the shear of the strong

anticyclones but also to the internal wave field. Quasi-stationary waves relative to the topography are likely to be observed in different frequency ranges and will partially contribute to the subinertial shear.

Tides may also be expected to affect turbulent dissipation at the western boundary. An approximate M_2 energy flux of $10^{-3}\,\mathrm{W\,m^{-2}}$ is found at the western boundary from an estimate of internal tide generation (Nycander 2005) based on linear wave theory. However, this energy flux is not sufficient to account for the difference of depth-integrated high-frequency kinetic energy estimated between anticyclones and cyclones ($390\,\mathrm{J\,m^{-2}}$; Fig. 7) during a tidal period and for a period shorter than ~5 days. The 2–3-month modulation of internal wave activity in the area is rather suggestive of an eddy-induced modulation of internal wave generation, while within the scope of the study, internal tides do not appear to modulate the shear variance (Fig. 6e).

The present calculation of the tidal effect on the kinetic energy based on the M_2 energy flux does not account for a potential link between anticyclones, internal tides, and high-frequency waves. This link could occur through resonant interactions between eddies and tides (Lelong and Kunze 2013); such an analysis would require further information, particularly on the horizontal wavelength of tides at the western boundary to estimate resonance conditions. Alternatively, eddies may
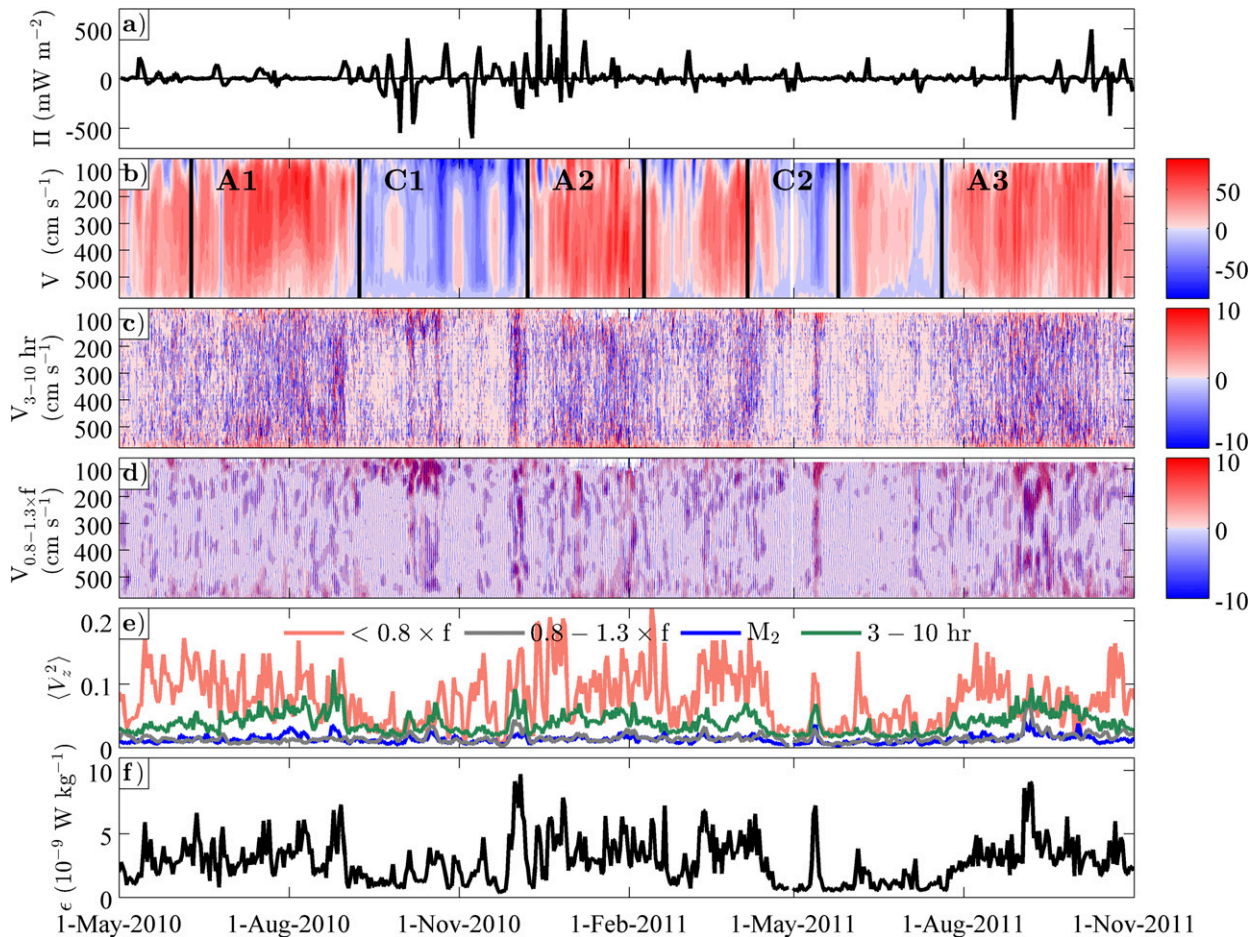
FIG. 6. (a) Energy flux into inertial motions calculated from a slab model at Wba. Vertical profile of meridional velocity at Wba: (b) 12-h sampled, (c) baroclinic velocity 3–10-h bandpass filtered, and (d) baroclinic velocity $(0.8–1.3) \times f$ (near inertial) bandpass filtered. (e) Shear variance of the subinertial (red), near-inertial (gray), M_2 (blue), and 3–10-h (green) bands. (f) Dissipation rate at Wba, averaged daily.

enhance internal wave dissipation through near-inertial wave trapping in the negative vorticity of anticyclonic eddy features (Kunze 1985).

2) PROPAGATION OF INTERNAL WAVES

In an effort to identify the direction of internal wave propagation and to confirm whether bottom-generated waves were responsible for the enhanced dissipation observed during anticyclones, we computed the vertical wavenumber rotary spectra (Gonella 1972) of buoyancy frequency–normalized shear variance following Sheen et al. (2013). The transition from anticyclone A1 to cyclone C1 is analyzed in Fig. 8, as it shows that the polarity of the eddy strongly affects the total, clockwise, and counterclockwise shear variance. The transition of eddy polarity based on the surface relative vorticity (vertical black line on 8 September) is slightly delayed compared with the presence of

intensified internal waves up to 1 September. Two wave packets of downward phase propagation are measured on 25 and 30 August 2010 for approximately 1 day in the 3–10-h bandpass-filtered velocities (Figs. 8b,c). These packets have a larger counterclockwise over clockwise component of shear variance (Fig. 8d), indicating upward group velocity and energy flux. The wave packets illustrate the result from the vertical wavenumber–frequency shear spectra (Fig. 4) and may characterize internal waves generated in the lee of the topographic rise. Despite the presence of several internal wave packets with upward propagating energy during anticyclones (Fig. 8), internal waves may be deflected by the large anticyclonic sheared flow, which may cause a vertical shift of the phase lines (Baines 1995) and affect the detection of their propagation direction.

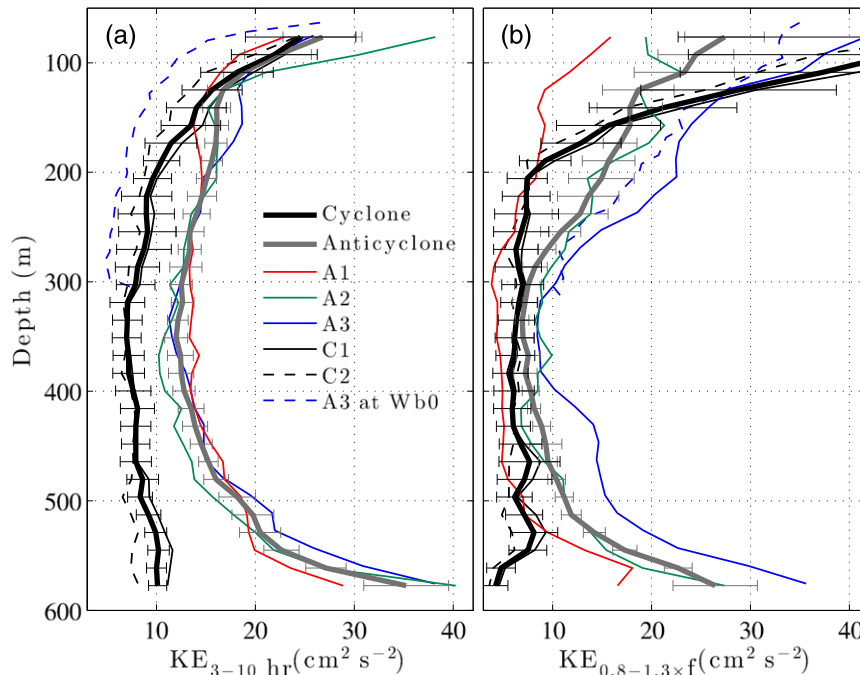To obtain some insight on the internal wave field, we display in Fig. 7 the vertical structure of the horizontal

FIG. 7. (a) High-frequency (3–10-h bandpass filtered) and (b) near-inertial [(0.8–1.3) × f bandpass filtered] horizontal kinetic energy at Wba averaged for the main three anticyclones (A1, A2, and A3) and the two cyclones (C1 and C2). The average structure and the 95% confidence intervals are indicated in bold gray and black for the anticyclone and cyclone, respectively. The anticyclone A3 is also sampled by the ADCP Wb0 above 300 m.

kinetic energy averaged for each of the large eddies at the site. Below 150 m, kinetic energy in anticyclones is intensified in the high-frequency (3–10 h) band relative to cyclones (Fig. 7a). The presence of high-frequency waves during anticyclones throughout the water column was also visible in Fig. 6c and is consistent with enhanced vertical wavenumber shear spectra for anticyclones at wavelengths of 67–500 m (Fig. 4). Energetic and shallow high-frequency waves during C1 (Fig. 6c) following a storm reduce the kinetic energy difference between anticyclones and cyclones near the surface.

The even stronger kinetic energy below 400 m compared with shallower depths may suggest a bottom generation mechanism. The origin of the enhancement of the mean energy for the anticyclones, alongside the large confidence intervals in the bottommost 150 m (Fig. 7a), may also involve another mechanism. This deep enhancement may relate to a boundary layer process as this region is shielded northward by the ∼300-m topographic rise (Figs. 1b,c). This hypothesis is further supported by the independence of the bottom enhanced energy to the two internal wave frequency bands (Fig. 7) or to a low-pass frequency band with a frequency lower than 1.3 × f.

In the near-inertial band, the kinetic energy differences between cyclones and anticyclones are absent at middepth (Fig. 7b). Because of the passage of two storms previously mentioned in the region (Tropical Storm Otto in October 2010 and Hurricane Irene in September 2011), the near-inertial energy in the shallowest 150 m is particularly intensified for C1 and A3; a direct link is not observed for the shallow energy peak of C2.

The extent of the effect of the topographic rise on the internal wave field is assessed by comparing the kinetic energy at Wba and Wb0 during their common period of measurement for anticyclone A3. From Figs. 1b and 1c, Wba (13 km offshore at 76.87°W) is oriented upstream of the topographic rise, whereas Wb0 (16 km offshore at 76.84°W) is no longer facing the tall topographic rise. The high-frequency kinetic energy averaged during anticyclone A3 at Wba and Wb0 in their common depth range (between 60 and 300 m), is less enhanced at Wb0 than at Wba below ∼150 m (Fig. 7). This suggests that the intensified generation of internal waves and their subsequent local propagation are mostly present over the topographic rise. Other bathymetric features found over the Blake Plateau northward of the topographic rise, such as the two steep escarpments at 26.63° and
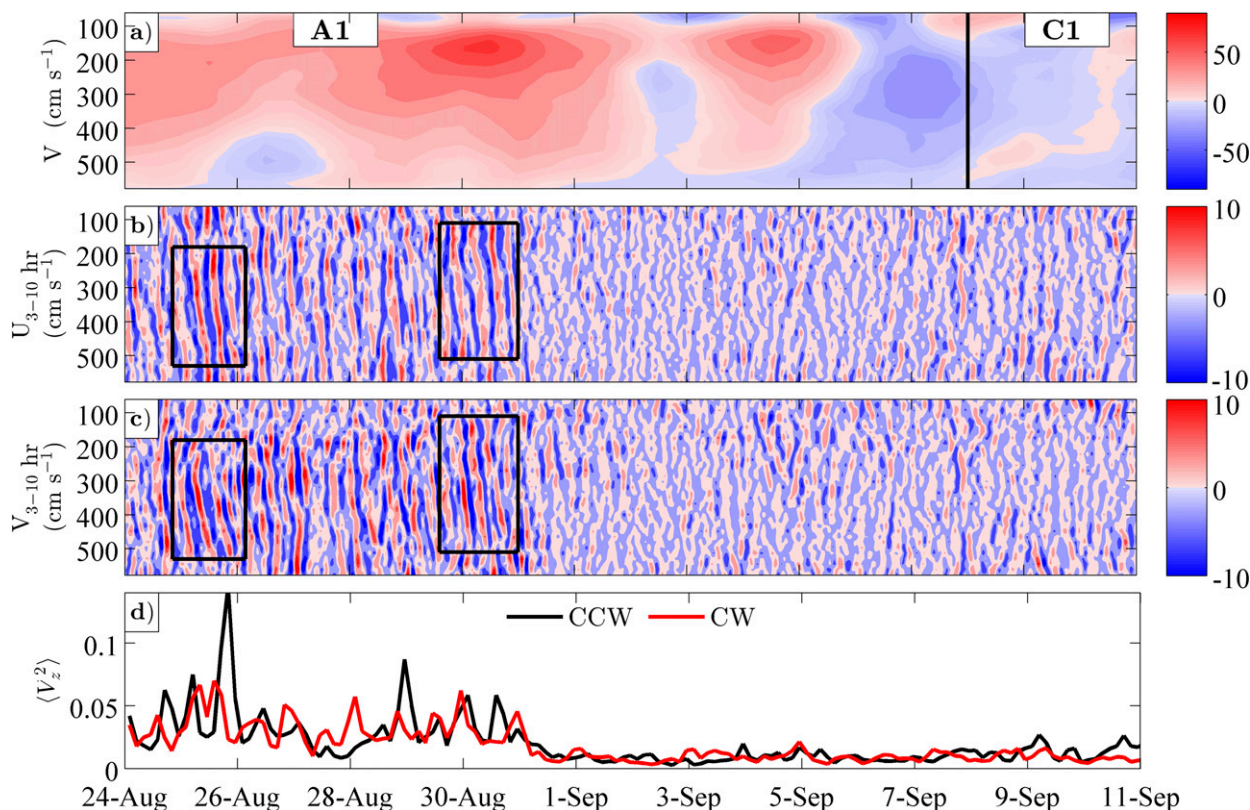
FIG. 8. (a) Vertical profile of the 12-h sampled meridional velocity at Wba, (b) zonal and (c) meridional baroclinic velocity 3–10-h bandpass-filtered, and (d) clockwise (red) and counterclockwise (black) components of the buoyancy frequency–normalized shear variance. This subset taken in 2010 represents the transition from anticyclone A1 to cyclone C1 delimited by the vertical black line in (a) based on the sign change of the surface relative vorticity. The two wave packets mentioned in the text are marked by black rectangles in (b),(c).

26.73°N, may also strongly contribute to the intensified internal wave field.

3) DISCUSSION ON THE INTERNAL WAVE GENERATION

Considering the observed enhancement of internal waves during northward bottom velocities and the apparent upward energy propagation of these waves, a potential mechanism for the generation of internal waves is discussed. However, because of the limited observations primarily deriving from a single 75-kHz ADCP, we will consider possible scalings and their consistency with the observations, rather than attempt to identify the controlling dynamics. The linear theory of lee wave generation (Bell 1975; Gill 1982) applies in the presence of a flow strong enough to overcome the topography and stratification, as defined by a subcritical inverse topographic Froude number ($Fr_{topo}^{-1} \ll 1$, where $Fr_{topo}^{-1} = NH/U$). In the nonlinear case ($Fr_{topo}^{-1} > 1$), the upstream flow is partially blocked, or can travel eastward as in the present topographic rise (Fig. 1), and instabilities can develop in the lee and upstream sides of

the topography, rendering the wave generation less predictable (Baines 1995; Klymak et al. 2010). In our case, despite being in the nonlinear regime (supercritical Fr_{topo}^{-1} ranging from 12 to 75, for velocities between 8 and $50 \, cm \, s^{-1}$), a regime of enhanced bottom velocity may be strong enough to generate waves over the shallowest section of the topographic rise.

The blocking depth, defined as U/N, ranges from 20 to 125 m in the presence of the low-frequency currents (8–$50 \, cm \, s^{-1}$). In this regime, a large portion of the upstream flow is blocked or can contribute to a horizontal flow separation (MacCready and Pawlak 2001). As underlined by Winters and Armi (2013), a rescaled topographic width of 0.8–3.5 km relates to the blocking depth. In the linear theory, the topographic width compares with the horizontal wavenumber k and predicts a frequency range $U \times k$ of 6.3–$9 \times 10^{-4} \, s^{-1}$ or a period of 2–3 h. This predicted frequency for the internal waves is not inconsistent with the lower limit of the observed range (3–10 h), suggesting that a linear lee wave generation mechanism may be involved in the generation of internal waves over the topographic rise.

4) EDDY-INDUCED MODULATION OF THE TURBULENT DISSIPATION RATE

Using the measured shear spectra, a time series of the turbulent dissipation rate at the western boundary may be obtained (Fig. 6e). As suggested by elevated spectral levels for higher near-bottom eddy flows (Fig. 5a), the dissipation rate is elevated in anticyclones. In the "weak" eddy velocity range $|v| < 8 \, \mathrm{cm \, s^{-1}}$, which is mostly representative of cyclonic flow (82% based on ζ/f), the dissipation rate is independent of the velocity (Fig. 9). The average and standard errors of the dissipation rate and diffusivity are $\varepsilon = (0.9 \pm 0.6) \times 10^{-9} \, \mathrm{W \, kg^{-1}}$ and $K_\rho = (1.2 \pm 0.8) \times 10^{-5} \, \mathrm{m^2 \, s^{-1}}$. For enhanced near-bottom eddy velocities of $8 < |v| < 50 \, \mathrm{cm \, s^{-1}}$, dissipation rates are higher, consistent with the notion of waves being generated beyond a velocity threshold for which the bottom flow is no longer entirely blocked but can cross the steep topographic rise $\varepsilon = (2.8 \pm 0.4) \times 10^{-9} \, \mathrm{W \, kg^1}$ and $K_\rho = (3.5 \pm 0.5) \times 10^{-5} \, \mathrm{m^2 \, s^{-1}}$.

5) EDDY DECAY

Having observed an enhanced dissipation rate around the topographic rise for anticyclones, we assess from the kinetic energy equation (Gill 1982) whether this level of dissipation may contribute to the decay of anticyclones. An average decay time scale τ is computed for the main anticyclones, with ρ being the mean density, as

$$\tau = \frac{\frac{1}{2} \int_V \rho(u^2 + v^2) \, dV}{\int_V \rho(1 + \Gamma)\varepsilon \, dV}. \tag{2}$$

A volume integral is estimated in cylindrical coordinates using the distance between Wba and Wb4 as radius and integrating from the surface to 1500 m the average depth of the Blake Plateau. An estimate of the volume-integrated dissipation rate for anticyclones ($3.9 \times 10^7 \, \mathrm{W}$) is obtained by assuming that internal wave generation and dissipation act over 20% of the eddy area (i.e., the portion of the eddy interacting with the Blake Plateau; Fig. 2). Given a volume-integrated kinetic energy characteristic of anticyclones ($1.9 \times 10^{14} \, \mathrm{J}$), which is at a maximum one month after the arrival of each anticyclone at the boundary (Fig. 3), a decay time scale of 55 days due to internal wave breaking is found. This decay time scale is comparable to the observed eddy decay time scale of 81 days (defined by the sign of ζ/f and confirmed by SSHA maps), and supports the hypothesis that internal wave generation contributes to eddy decay at the western boundary. The contribution of the internal wave field to the decay of anticyclones
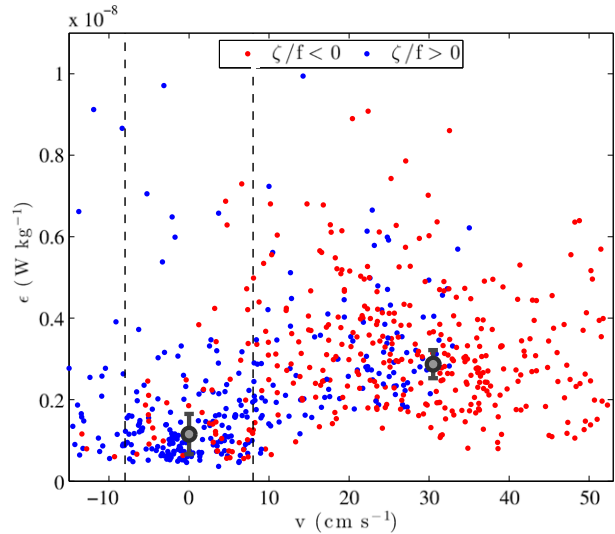

FIG. 9. Turbulent energy dissipation rate ε vs meridional velocity of the deepest 100 m at Wba for anticyclones (red) and cyclones (blue). The thick black–gray circled points with vertical bars indicate the median and standard error of the dissipation rate for each interval marked by $|v| = 8 \, \mathrm{cm \, s^{-1}}$ (dashed vertical lines).

may be at odds with the apparent independence of the eddy decay rate (as observed from altimetry) with respect to eddy polarity. Further work is needed to clarify this possible inconsistency, which may also relate to the lower kinetic energy level of cyclones relative to anticyclones (Figs. 2d–f and Fig. 3d). To improve our understanding of eddy energy budgets, the importance of the internal wave generation in the eddy decay needs to be quantified relative to other processes, for example, bottom drag, eddy energy exchange between eddies of opposite polarities, or local eddy energy dissipation via nonlinear processes, which are likely to be important near the topographic ridge.

4. Conclusions

In situ velocity measurements and satellite altimetric observations at the western boundary of the North Atlantic at 26.5°N provide evidence that the local internal wave field is modulated by mesoscale eddies impinging on the boundary. In particular, anticyclonic eddies with substantial near-bottom flow are associated with elevated internal wave shear variance and turbulent dissipation, relative to cyclonic eddies. The intensified anticyclonic high-frequency energy below ~150 m and the upward energy propagation of high-frequency waves support a bottom generation mechanism. The estimated level of dissipation, when applied to the portion of the eddy in contact with the boundary, suggests that the eddy-induced generation of internal

waves contributes to draining energy from the mesoscale eddy field at the western boundary. This work calls for a targeted investigation of these processes in the region that may define the prevailing mechanism by which eddy impingement leads to the generation of internal waves. A study of the internal wave propagation may establish the eddy-induced effect on the local hydrography and tracer concentrations as well as the effect on the deep mixing and circulation at the western boundary.

REFERENCES

Baines, P. G., 1995: *Topographic Effects in Stratified Flows.* Cambridge University Press, 500 pp.

Bell, T. H., 1975: Lee waves in stratified flows with simple harmonic time dependence. *J. Fluid Mech.*, **67**, 705–722, doi:10.1017/S0022112075000560.

Brearley, J. A., K. L. Sheen, A. C. Naveira Garabato, D. A. Smeed, and S. Waterman, 2013: Eddy-induced modulation of turbulent dissipation over rough topography in the Southern Ocean. *J. Phys. Oceanogr.*, **43**, 2288–2308, doi:10.1175/JPO-D-12-0222.1.

Bryden, H. L., W. E. Johns, and P. M. Saunders, 2005: Deep western boundary current east of Abaco: Mean structure and transport. *J. Mar. Res.*, **63**, 35–57, doi:10.1357/0022240053693806.

Bühler, O., and M. E. McIntyre, 2005: Wave capture and wave-vortex duality. *J. Fluid Mech.*, **534**, 67–95, doi:10.1017/S0022112005004374.

Clément, L., E. Frajka-Williams, Z. B. Szuts, and S. A. Cunningham, 2014: Vertical structure of eddies and Rossby waves, and their effect on the Atlantic meridional overturning circulation at 26.5°N. *J. Geophys. Res.*, **119**, 6479–6498, doi:10.1002/2014JC010146.

Cunningham, S. A., and Coauthors, 2007: Temporal variability of the Atlantic meridional overturning circulation at 26.5°N. *Science*, **317**, 935–938, doi:10.1126/science.1141304.

D'Asaro, E. A., 1985: The energy flux from the wind to near-inertial motions in the surface mixed layer. *J. Phys. Oceanogr.*, **15**, 1043–1059, doi:10.1175/1520-0485(1985)015<1043:TEFFTW>2.0.CO;2.

Dee, D. P., and Coauthors, 2011: The ERA-Interim reanalysis: Configuration and performance of the data assimilation system. *Quart. J. Roy. Meteor. Soc.*, **137**, 553–597, doi:10.1002/qj.828.

Ferrari, R., and C. Wunsch, 2009: Ocean circulation kinetic energy: Reservoirs, sources, and sinks. *Annu. Rev. Fluid Mech.*, **41**, 253–282, doi:10.1146/annurev.fluid.40.111406.102139.

Frajka-Williams, E., W. E. Johns, C. S. Meinen, L. M. Beal, and S. A. Cunningham, 2013: Eddy impacts on the Florida Current. *Geophys. Res. Lett.*, **40**, 349–353, doi:10.1002/grl.50115.

Gill, A. E., 1982: *Atmosphere-Ocean Dynamics.* International Geophysics Series, Vol. 30, Academic Press, 662 pp.

——, J. S. A. Green, and A. J. Simmons, 1974: Energy partition in the large-scale ocean circulation and the production of mid-ocean eddies. *Deep-Sea Res. Oceanogr. Abstr.*, **21**, 499–528, doi:10.1016/0011-7471(74)90010-2.

Gonella, J., 1972: A rotary-component method for analysing meteorological and oceanographic vector time series. *Deep-Sea Res. Oceanogr. Abstr.*, **19**, 833–846, doi:10.1016/0011-7471(72)90002-2.

Gregg, M. C., 1989: Scaling turbulent dissipation in the thermocline. *J. Geophys. Res.*, **94**, 9686–9698, doi:10.1029/JC094iC07p09686.

——, and E. Kunze, 1991: Shear and strain in Santa Monica Basin. *J. Geophys. Res.*, **96**, 16 709–16 719, doi:10.1029/91JC01385.

——, T. B. Sanford, and D. P. Winkel, 2003: Reduced mixing from the breaking of internal waves in equatorial ocean waters. *Nature*, **422**, 513–515, doi:10.1038/nature01507.

Henyey, F. S., J. Wright, and S. M. Flatté, 1986: Energy and action flow through the internal wave field: An eikonal approach. *J. Geophys. Res.*, **91**, 8487–8495, doi:10.1029/JC091iC07p08487.

Hogg, A. M., W. K. Dewar, P. Berloff, and M. L. Ward, 2011: Kelvin wave hydraulic control induced by interactions between vortices and topography. *J. Fluid Mech.*, **687**, 194–208, doi:10.1017/jfm.2011.344.

Johns, W. E., L. M. Beal, M. O. Baringer, J. R. Molina, S. A. Cunningham, T. Kanzow, and D. Rayner, 2008: Variability of shallow and deep western boundary currents off the Bahamas during 2004–05: Results from the 26°N RAPID-MOC array. *J. Phys. Oceanogr.*, **38**, 605–623, doi:10.1175/2007JPO3791.1.

Klymak, J. M., S. Legg, and R. Pinkel, 2010: High-mode stationary waves in stratified flow over large obstacles. *J. Fluid Mech.*, **644**, 321–336, doi:10.1017/S0022112009992503.

Köhler, J., C. Mertens, M. Walter, U. Stöber, M. Rhein, and T. Kanzow, 2014: Variability in the internal wave field induced by the Atlantic Deep Western Boundary Current at 16°N. *J. Phys. Oceanogr.*, **44**, 492–516, doi:10.1175/JPO-D-13-010.1.

Kunze, E., 1985: Near inertial-wave propagation in geostrophic shear. *J. Phys. Oceanogr.*, **15**, 544–565, doi:10.1175/1520-0485(1985)015<0544:NIWPIG>2.0.CO;2.

——, E. Firing, J. M. Hummon, T. K. Chereskin, and A. M. Thurnherr, 2006: Global abyssal mixing inferred from lowered ADCP shear and CTD strain profiles. *J. Phys. Oceanogr.*, **36**, 1553–1576, doi:10.1175/JPO2926.1.

Lee, T. N., W. E. Johns, R. J. Zantopp, and E. Fillenbaum, 1996: Moored observations of western boundary current variability and thermohaline circulation at 26.5°N in the subtropical North Atlantic. *J. Phys. Oceanogr.*, **26**, 962–983, doi:10.1175/1520-0485(1996)026<0962:MOOWBC>2.0.CO;2.

Lelong, M.-P., and E. Kunze, 2013: Can barotropic tide–eddy interactions excite internal waves? *J. Fluid Mech.*, **721**, 1–27, doi:10.1017/jfm.2013.1.

Liang, X., and A. M. Thurnherr, 2012: Eddy-modulated internal waves and mixing on a midocean ridge. *J. Phys. Oceanogr.*, **42**, 1242–1248, doi:10.1175/JPO-D-11-0126.1.

MacCready, P., and G. Pawlak, 2001: Stratified flow along a corrugated slope: Separation drag and wave drag. *J. Phys. Oceanogr.*, **31**, 2824–2839, doi:10.1175/1520-0485(2001)031<2824:SFAACS>2.0.CO;2.

Naveira Garabato, A. C., K. L. Polzin, B. A. King, K. J. Heywood, and M. Visbeck, 2004: Widespread intense turbulent mixing in the Southern Ocean. *Science*, **303**, 210–213, doi:10.1126/science.1090929.

Nikurashin, M., and R. Ferrari, 2010: Radiation and dissipation of internal waves generated by geostrophic motions impinging on small-scale topography: Application to the Southern Ocean. *J. Phys. Oceanogr.*, **40**, 2025–2042, doi:10.1175/2010JPO4315.1.

Nycander, J., 2005: Generation of internal waves in the deep ocean by tides. *J. Geophys. Res.*, **110**, C10028, doi:10.1029/2004JC002487.

Osborn, T. R., 1980: Estimates of the local rate of vertical diffusion from dissipation estimates. *J. Phys. Oceanogr.*, **10**, 83–89, doi:10.1175/1520-0485(1980)010<0083:EOTLRO>2.0.CO;2.

Pollard, R. T., and R. C. Millard, 1970: Comparison between observed and simulated wind-generated inertial oscillations. *Deep-Sea Res. Oceanogr. Abstr.*, **17**, 813–821, doi:10.1016/0011-7471(70)90043-4.

Polzin, K. L., 2008: Mesoscale eddy–internal wave coupling. Part I: Symmetry, wave capture and results from the Mid-Ocean Dynamics Experiment. *J. Phys. Oceanogr.*, **38**, 2556–2574, doi:10.1175/2008JPO3666.1.

——, 2010: Mesoscale eddy–internal wave coupling. Part II: Energetics and results from PolyMode. *J. Phys. Oceanogr.*, **40**, 789–801, doi:10.1175/2009JPO4039.1.

——, J. M. Toole, and R. W. Schmitt, 1995: Finescale parameterizations of turbulent dissipation. *J. Phys. Oceanogr.*, **25**, 306–328, doi:10.1175/1520-0485(1995)025<0306:FPOTD>2.0.CO;2.

——, A. C. Naveira Garabato, T. N. Huussen, B. M. Sloyan, and S. Waterman, 2014: Finescale parameterizations of turbulent dissipation. *J. Geophys. Res.*, **119**, 1383–1419, doi:10.1002/2013JC008979.

Salmon, R., 1978: Two-layer quasi-geostrophic turbulence in a simple special case. *Geophys. Astrophys. Fluid Dyn.*, **10**, 25–52, doi:10.1080/03091927808242628.

Scott, R. B., and F. Wang, 2005: Direct evidence of an oceanic inverse kinetic energy cascade from satellite altimetry. *J. Phys. Oceanogr.*, **35**, 1650–1666, doi:10.1175/JPO2771.1.

Sen, A., R. B. Scott, and B. K. Arbic, 2008: Global energy dissipation rate of deep-ocean low-frequency flows by quadratic bottom boundary layer drag: Computations from current-meter data. *Geophys. Res. Lett.*, **35**, L09606, doi:10.1029/2008GL033407.

Sheen, K. L., and Coauthors, 2013: Rates and mechanisms of turbulent dissipation and mixing in the Southern Ocean: Results from the DIMES experiment. *J. Geophys. Res. Oceans*, **118**, 2774–2792, doi:10.1002/jgrc.20217.

St. Laurent, L., A. C. Naveira Garabato, J. R. Ledwell, A. M. Thurnherr, J. M. Toole, and A. J. Watson, 2012: Turbulent and diapycnal mixing in Drake Passage. *J. Phys. Oceanogr.*, **42**, 2143–2152, doi:10.1175/JPO-D-12-027.1.

Vallis, G. K., 2006: *Atmospheric and Oceanic Fluid Dynamics*. Cambridge University Press, 745 pp.

Waterman, S., A. C. Naveira Garabato, and K. L. Polzin, 2013: Internal waves and turbulence in the Antarctic Circumpolar Current. *J. Phys. Oceanogr.*, **43**, 259–282, doi:10.1175/JPO-D-11-0194.1.

Winters, K. B., and L. Armi, 2013: The response of a continuously stratified fluid to an oscillating flow past an obstacle. *J. Fluid Mech.*, **727**, 83–118, doi:10.1017/jfm.2013.247.

Wunsch, C., 1998: The work done by the wind on the oceanic general circulation. *J. Phys. Oceanogr.*, **28**, 2332–2340, doi:10.1175/1520-0485(1998)028<2332:TWDBTW>2.0.CO;2.

Zhai, X., H. L. Johnson, and D. P. Marshall, 2010: Significant sink of ocean-eddy energy near western boundaries. *Nat. Geosci.*, **3**, 608–612, doi:10.1038/ngeo943.